Impact of permeable conduits on solute transport in aquitards: Mathematical models and their application

Glenn A. Harrington,[1,2] M. Jim Hendry,[2] and Neville I. Robinson[3]

Received 28 March 2005; revised 16 October 2006; accepted 20 February 2007; published 26 May 2007.

[1] The migration of contaminants through porous conduits (for example, sand layers) in aquitards, or any preferential flow feature within a low-permeability matrix, can be significantly retarded via diffusion into the matrix and processes such as sorption and decay. Previous solutions for simulating contaminant transport in these types of environments have been limited to a parallel-plate approach such as that used in studies of fractured rock aquifers. A major drawback of using these approaches is that they cannot account for the radial component of diffusion that occurs from circular- or elliptical-sectioned conduits. We have developed solutions for both of the latter cases and compared results from generic simulations to those obtained with a conventional parallel-plate model. The results demonstrated using a circular conduit approach can produce concentration profiles for both the conduit and surrounding matrix that are up to several orders of magnitude lower than those predicted using parallel-plate models. The solutions for elliptical-section conduits provide concentration profiles that are bounded by the circular- and parallel-plate models. We also present several generic simulations to demonstrate the effects of conduit radius and average groundwater flow velocity on concentration profiles. Finally, the circular conduit model is applied to a clay-rich till aquitard in southern Saskatchewan, Canada to provide insight into an anomalous dissolved chloride peak in the vertical pore water profile. The model demonstrates that the source of the high Cl^- could be as far as 10–100 km from the site (although this distance may be unrealistic) and allows estimation of the Cl^- concentration at the source. We envisage that the solutions for conduit diffusion will have far wider applications than just aquitard studies, and future uses may include tracer tests in karstic and fractured aquifers.

Citation: Harrington, G. A., M. J. Hendry, and N. I. Robinson (2007), Impact of permeable conduits on solute transport in aquitards: Mathematical models and their application, *Water Resour. Res.*, *43*, W05441, doi:10.1029/2005WR004144.

1. Introduction

[2] The ability of an aquitard to isolate hazardous waste or to protect underlying aquifers from contamination is often controlled by the presence of physical heterogeneity. Surface fractures and faults can significantly enhance the infiltration rate of water and its chemical constituents through what are otherwise very low permeability (K typically $< 10^{-9}$ ms^{-1}) clay-rich tills [*Hendry*, 1982; *McKay et al.*, 1993; *Gerber et al.*, 2001]. Numerical discrete-fracture models were developed by *Harrison et al.* [1992] and *Jørgensen et al.* [2004] to assess the importance of various scales of aquitard fracturing on contaminant transport to underlying aquifers. Both studies demonstrated that deep, widely spaced fractures with apertures <100 μm could facilitate contamination of an aquifer beneath ~15 m of clay-rich till. The natural attenuation properties of aquitards, including their capacity for diffusion and chemical sorption, will, however, retard contaminant migration along fractures, faults, and any other high-permeability features (for example, sand layers). Over the last three decades there have been many studies of solute transport between semi-infinite parallel plates [e.g., *Grisak and Pickens*, 1980; *Lever and Bradbury*, 1985; *Neretnieks*, 1980, 1981; *Maloszewski and Zuber*, 1985, 1990, 1991; *Sudicky and Frind*, 1981, 1982; *Tang et al.*, 1981, and many citations of these papers]. These approaches allow the simulation and prediction of solute concentration distributions in either fractured-rock aquifers or classical confined aquifers and can account for processes such as matrix diffusion, chemical sorption, and radioactive decay.

[3] Despite this wealth of literature on contaminant transport phenomena in fractured geologic media, it appears that there have been no studies on the radial diffusive loss of solute mass from conduits of finite cross sections. The transport of contaminants along a circular-sectioned, porous conduit will produce concentration "halos" in the surrounding aquitard in the same way that concentration profiles develop in porous, fractured rocks. However, there is an expectation that concentration levels around conduits of circular or other finite cross sections would be different

[1]Department of Water, Land and Biodiversity Conservation, Mount Gambier, Australia.
[2]Department of Geological Sciences, University of Saskatchewan, Saskatoon, Canada.
[3]School of Chemistry, Physics and Earth Sciences, Flinders University, Adelaide, Australia.

0043-1397/07/2005WR004144

from the parallel-plate models and that these latter models may be inadequate for simulating solute distribution in finite-sectioned conduits and the surrounding aquitard.

[4] Sand-filled channel deposits are ideal for transmitting contaminants through aquitards and are commonly encountered in glacial tills [e.g., *Hendry et al.*, 2004; *Gerber et al.*, 2001]. Even under low hydraulic gradients ($i = 10^{-4}$ to 10^{-3}), these depositional features can have such high hydraulic conductivities ($K = 10^{-3}$ to 10^{-2} m s^{-1}) that the average groundwater velocity within them can be on the order of 10^2 to 10^3 m yr^{-1}. Thus it is crucial for groundwater managers to have tools to study contaminant transport in these high-permeability conduits.

[5] The main objective of the current study was to develop new models to answer questions such as the following: How close does one have to be to these high-permeability features in order to see evidence of the natural or anthropogenic contaminants they are transporting? Alternatively, how far do contaminants penetrate the surrounding aquitard at different distances and traveltimes from the source? Finally, what is the difference between solute concentration profiles predicted using circular-section conduit models and traditional parallel-plate models bridged by elliptical-section conduit models? Also, the availability of new semi-analytical solutions would provide valuable benchmarks for numerical methods such as finite differences and finite elements.

[6] The final objective of this study was to apply the new models to a field site in southern Saskatchewan, Canada. The King site has been a focal point for aquitard research over the last 10 years and has enhanced our understanding of the complex physical and chemical behavior of these systems. Previous studies at the site have primarily concentrated on estimating geotechnical/hydraulic properties for the clay-rich till [*Shaw and Hendry*, 1998; *Boldt-Leppin and Hendry*, 2003] and interpreting one-dimensional chemical and isotopic profiles [e.g., *Hendry and Wassenaar*, 1999, 2000; *Wassenaar and Hendry*, 2000; *Hendry et al.*, 2000; *Vengosh and Hendry*, 2001]. In this paper, we investigate the role of physical heterogeneity (sand layers) on solute transport through the till. A sand deposit has been identified at approximately 10–15 m below ground (BG) using drill cuttings/core [*Shaw*, 1997], direct-push EC logging [*Harrington and Hendry*, 2005, 2006] and pore water Cl^- profiles [*Hendry et al.*, 2000]. By studying the manner in which these sand features have influenced, and will continue to influence, solute migration through the aquitard, we were able to predict contaminant behavior in other similar hydrogeological settings.

2. Transport Models for Conduit and Aquitard

[7] The sequence of this section is first to present the concentration transport equations for a solute moving through a conduit of arbitrary cross section and containing a porous medium such as sand with diffusional migration through the surrounding aquitard. Laplace transformation of time dependence of concentrations is then applied to all equations. At this stage the arbitrariness of cross-sectional shape is restricted to circles, ellipses, and parallel lines. Analytical solutions for these shapes are then determined in the Laplace transform domain. Finally, Laplace transform inversion to the real-time domain is achieved by robust numerical methods.

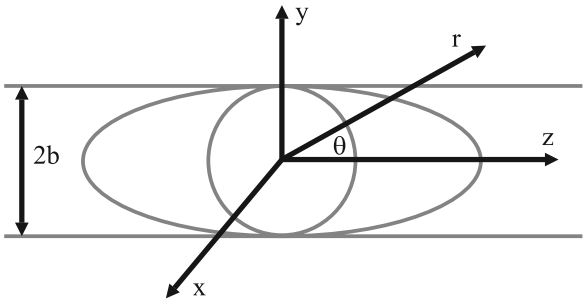

Figure 1. Coordinate systems used for three conduit cross sections as circles, ellipses, and parallel lines.

2.1. Transport Equations for Matrix and Conduit of Arbitrary Section

[8] Here we use the more general term of matrix rather than aquitard to emphasize the generality of application.

[9] Consider the conduit to be a cylinder of arbitrary cross section with an area Ω and perimeter Γ carrying solute, which is sufficiently well mixed that the concentration $C_c = C_c(x, t)$ is constant throughout the cross section. Here x is the axial coordinate of the conduit and t is time. The one-dimensional mass balance equation of a section of conduit of thickness dx is

$$\phi_c \Omega dx R_c \frac{\partial C_c}{\partial t} = \phi_c \left(D_c \frac{\partial^2 C_c}{\partial x^2} - v \frac{\partial C_c}{\partial x} - \lambda R_c C_c \right) \Omega dx + dx \phi_m D_m \int_\Gamma \frac{\partial C_m}{\partial n} ds \quad (1)$$

The additional definitions of quantities appearing in equation (1) are as follows. ν is the average groundwater velocity in the x direction ($L.T^{-1}$); D_c is the coefficient of hydrodynamic dispersion for the conduit ($D_c = \alpha_L \nu + D_{ce}$ where α_L is longitudinal dispersivity (L) and D_{ce} is effective diffusion coefficient for the conduit [$L^2.T^{-1}$]); λ is a first-order decay constant (T^{-1}); R_c is the face retardation coefficient for the conduit (equivalent to that defined by *Tang et al.* [1981]); ϕ_c and ϕ_m are the porosities of the conduit and matrix, respectively (−) ($\phi_c = 1$ for an open conduit); D_m is the effective diffusion coefficient for the matrix [$L^2.T^{-1}$]; $C_m = C_m(x, r, \theta, t)$ is the matrix concentration with polar coordinates (r, θ) originating from a central axis of the conduit (Figure 1; later these will be specialized to elliptical and Cartesian coordinates); n is the coordinate for the outward normal (L) to the boundary Γ, and s is the arc coordinate (L) along Γ in a counterclockwise direction.

[10] Dividing throughout equation (1) by $\phi_c D_c \Omega$ dx yields the conduit one-dimensional transport equation for an arbitrary section,

$$\frac{\partial^2 C_c}{\partial x^2} - \frac{v}{D_c}\frac{\partial C_c}{\partial x} - \lambda \frac{R_c}{D_c} C_c + \frac{\phi_m D_m}{\phi_c D_c \Omega} \int_\Gamma \frac{\partial C_m}{\partial n} ds = \frac{R_c}{D_c}\frac{\partial C_c}{\partial t} \quad (2)$$

[11] The two-dimensional equation for diffusion through Γ into the matrix is given by

$$\nabla^2 C_m - \lambda \frac{R_m}{D_m} C_m = \frac{R_m}{D_m} \frac{\partial C_m}{\partial t} \tag{3}$$

where R_m is the matrix retardation coefficient. The two-dimensional Laplacean, ∇^2, will be defined below in polar and elliptical coordinates.

[12] We consider the conduit to be of infinite length, initially the solute concentration being zero everywhere at $t = 0$ and, for $t > 0$, the conduit concentration at entry $x = 0$ is C_0. Mathematically, these conditions become Initial conditions:

$$C_c(x,0) = 0, \qquad C_m(x,r,\theta,0) = 0 \tag{4}$$

Boundary conditions, $t > 0$:

$$C_c(0,t) = C_0, \quad C_c(\infty,t) = 0, \quad C_m(x,\infty,\theta,t) = 0 \tag{5}$$

These are the simplest of boundary conditions for the conduit, which can be easily generalized when the conduit is of finite length and the input concentration is different, as for a pulse function. Additionally, there is the interface condition on Γ,

$$C_m = C_c \tag{6}$$

2.2. Laplace Transformation of Equations

[13] The Laplace transforms of C_c and C_m are now defined by

$$\{U_c,\ U_m\} = \mathcal{L}\{C_c,\ C_m\} = \int_0^\infty e^{-pt}\{C_c,\ C_m\}\mathrm{d}t \tag{7}$$

Taking the Laplace transforms of equations (2) and (3) together with the initial conditions (4) produces, first, the transformed differential equation for the conduit

$$\frac{\mathrm{d}^2 U_c}{\mathrm{d}x^2} - \frac{v}{D_c}\frac{\mathrm{d}U_c}{\mathrm{d}x} - (\lambda + p)\frac{R_c}{D_c}U_c + \frac{\phi_m D_m}{\phi_c D_c \Omega}\int_\Gamma \frac{\partial U_m}{\partial n}\mathrm{d}s = 0 \tag{8}$$

Some new variables are now introduced to set equation (8) in a more compact form. Define a length w and matrix flux factor f by

$$w = \frac{\Omega}{\int_\Gamma \mathrm{d}s}, \qquad f = \frac{\phi_m D_m}{\phi_c D_c}\frac{1}{w} \tag{9}$$

In that the transformed boundary condition $U_m = U_c$ implies that, $U_m \propto U_c$ for all (r, θ), it is advantageous to introduce U_m^* defined by

$$U_m = -U_c\, U_m^* \tag{10}$$

Finally, set

$$\beta^2 = (\lambda + p)\frac{R_c}{D_c} + f\frac{\int_\Gamma \frac{\partial U_m^*}{\partial n}\mathrm{d}s}{\int_\Gamma \mathrm{d}s} \tag{11}$$

Equation (8) can now be written as

$$\frac{\mathrm{d}^2 U_c}{\mathrm{d}x^2} - \frac{v}{D_c}\frac{\mathrm{d}U_c}{\mathrm{d}x} - \beta^2 U_c = 0 \tag{12}$$

[14] The Laplace transformed matrix equation is simply the modified Helmholtz equation

$$\nabla^2 U_m - \alpha_m^2 U_m = 0 \tag{13}$$

where

$$\alpha_m^2 = (\lambda + p)\frac{R_m}{D_m} \tag{14}$$

Together with the differential equations (12) and (13), there are the transformed boundary conditions:

$$U_c(0) = \frac{C_0}{p}, \qquad U_c(\infty) = 0, \qquad U_m(x,\infty,\theta) = 0 \tag{15}$$

For convenience, the inclusions of the Laplace transform variable p in U_c and U_m have been suppressed.

2.3. General Solution of the Conduit Equation for U_c

[15] The effect on the conduit equation (12) of the shape of the conduit cross section is contained in the parameter β^2. This, however, does not prevent solving the conduit equation in general form as

$$U_c = \frac{C_0}{p} e^{(v/(2D_c)-\alpha_c)x} \tag{16}$$

where

$$\alpha_c = \sqrt{\frac{v^2}{4D_c^2} + \beta^2} \tag{17}$$

[16] If the length of the conduit were finite, the general solution for U_c would be $\exp(\nu/(2D_c)x)$ [A cosh $\alpha_c\, x$ + B sinh$\alpha_c\, x$], where the coefficients A and B are easily found from the boundary conditions at each end of the conduit [e.g., *Robinson and Sharp*, 1997; *Robinson et al.*, 1998].

2.4. Specific Solutions of Conduit Equations for U_c and Matrix Equations for U_m

[17] With specialization of conduit cross sections to circles, ellipses, and parallel lines, equation (13), with transformed boundary conditions, can be solved analytically for U_m. The shape quantities, Ω, $\int_\Gamma ds$, w, within f and required in β^2, can also be found. Each cross-sectional shape will now be considered in turn.

2.4.1. Circular Cross Section

[18] The natural coordinate system is polar, but because of angular symmetry only the radial coordinate is required. The Laplacean becomes

$$\nabla^2 = \frac{d^2}{dr^2} + \frac{1}{r}\frac{d}{dr} \tag{18}$$

With b, the radius of the circle, the solution of equation (13) is

$$U_m = U_c \frac{K_0(\alpha_m r)}{K_0(\alpha_m b)} \tag{19}$$

where K_0 ( ) is the modified Bessel function of the second kind and order 0. $K_0(\alpha_m r) \to 0$ as $r \to \infty$, as required by the far field boundary condition of equation (15).

[19] The shape parameters are

$$\Omega = \pi b^2, \qquad \int_\Gamma ds = 2\pi b, \qquad w = \frac{b}{2} \tag{20}$$

and the boundary integrals ratio is

$$\frac{\int_\Gamma \frac{\partial U_m^*}{\partial n} ds}{\int_\Gamma ds} = \left.\frac{dU_m^*}{dr}\right|_{r=b} = \alpha_m \frac{K_1(\alpha_m b)}{K_0(\alpha_m b)} \tag{21}$$

K_1 ( ) is the modified Bessel function of the second kind and of order 1.

2.4.2. Elliptical Cross Section

[20] The appropriate coordinate system for analytical solutions of an elliptical boundary problem is naturally elliptical. Consider the boundary Γ having the equation for an ellipse in standard Cartesian form, $z^2/a^2 + y^2/b^2 = 1$. The transformation from Cartesian coordinates (z, y) to elliptical coordinates (ξ, η), by $z = h \cosh \xi \cos \eta$, $y = h \sinh \xi \sin \eta$, $r^2 = h^2 (\cosh 2\xi + \cos 2\eta)/2$, $\theta = \tan^{-1}(\tanh \xi \tan \eta)$, with $h = \sqrt{a^2 - b^2}$, $a \geq b$, produces ellipses with constant ξ values and orthogonal hyperbolae with constant η values. On the boundary, Γ, $\xi = \xi_0 = \cosh^{-1}(a/h) = 1/2 \log [(a + b)/(a - b)]$. The Laplacean, in elliptical coordinate form [e.g., *McLachlan*, 1947] is

$$\nabla^2 = \frac{2}{h^2(\cosh 2\xi - \cos 2\eta)} \left(\frac{\partial^2}{\partial \xi^2} + \frac{\partial^2}{\partial \eta^2} \right) \tag{22}$$

The solution of equation (13) with this form of ∇^2 and associated boundary conditions (15) is nonstandard. Historically, there has been much work devoted to problems defined within an ellipse for the wave equation [e.g., *McLachlan*, 1947]. There have been a few papers devoted to transport in porous media focusing on problems in the petroleum industry of wells in petroleum reservoirs of elliptical shape or anisotropic permeabilities or fractures which intersect wells along their length [e.g., *Kucuk and Brigham*, 1979; *Obut and Ertigen*, 1987; *Spath and Thambynayagam*, 1997; *Stanislav et al.*, 1987, 1992]. However, we have neither found solutions to hydrogeological problems involving elliptical geometries and transient behavior nor to other applications that solve the problem at hand. In consequence, details of the solution are given in the Appendix using the notation and essential elements of the problem outlined by *McLachlan* [1947]. The main results are

$$U_m = U_c \sum_{m=0}^{\infty} (-1)^m A_0^{(2m)} \cdot \left\{ \frac{\sum_{j=0}^{\infty} A_{2j}^{(2m)} \left[I_j(v_1(\xi)) + K_j(v_2(\xi)) \right]}{\sum_{j=0}^{\infty} A_{2j}^{(2m)} I_j(v_1(\xi_0)) K_j(v_1(\xi_0))} \right\} ce_{2m}(\eta, -q) \tag{23}$$

As defined in the Appendix, $ce_{2m}(\eta, -q)$ is a bounded, oscillatory Mathieu function, $q = \alpha_m^2 h^2/4$, $\nu_1(\xi) = \sqrt{q} \exp(-\xi)$, $\nu_2(\xi) = \sqrt{q} \exp(\xi)$, and determinate coefficients are $A_{2j}^{(2m)}$. I_j ( ) and K_j ( ) are, respectively, modified Bessel functions of first and second kinds and order j. It is shown in the Appendix that $U_m \to 0$ as $\xi \to \infty$, as required.

[21] The shape parameters are

$$\Omega = \pi ab, \qquad \int_\Gamma ds = 4aE\left(\sqrt{1 - b^2/a^2}\right), \qquad w = \frac{\pi b}{4E\left(\sqrt{1 - b^2/a^2}\right)} \tag{24}$$

with E( ) as the complete elliptic integral of the second kind. When $a = b$, $E(0) = \pi/2$ and the above parameters reduce to those of the circle. The flux integral derived in the Appendix is

$$\int_\Gamma \frac{\partial U_m^*}{\partial n} ds = 4\pi \sum_{m=0}^{\infty} \left[A_0^{(2m)} \right]^2 \cdot \left\{ \frac{\sum_{j=0}^{\infty} A_{2j}^{(2m)} \left[v_1(\xi_0) I_{j+1}(v_1(\xi_0)) + v_2(\xi_0) K_{j+1}(v_2(\xi_0)) \right]}{\sum_{j=0}^{\infty} A_{2j}^{(2m)} I_j(v_1(\xi_0)) K_j(v_1(\xi_0))} \right\} \tag{25}$$

[22] Numerical computations necessitate the truncation of the infinite series. As indicated in the Appendix the number of terms required for high accuracy is not large.

2.4.3. Parallel Lines

[23] For parallel lines, $2b$ apart, coordinate y normal to the lines, the two-dimensional problem degenerates to a one-dimensional problem, with

$$\nabla^2 \to \frac{d^2}{dy^2} \tag{26}$$

and the solution for U_m is simply

$$U_m = U_c e^{-\alpha_m (y - b)} \tag{27}$$

This solution gives $U_c \to 0$ as $y \to \infty$, corresponding to the Cartesian form $C_m(x, y, z, t) \to C_m(x, y, t)_{y \to \infty} = 0$.

[24] A simple way to obtain w is to consider a rectangular conduit of depth $2b$ and width $2a$ and then let $a \to \infty$, so that

$$w = \frac{\Omega}{\int_\Gamma ds} = \left.\frac{4ab}{4(a + b)}\right|_{a \to \infty} = b \tag{28}$$

and

$$\left.\frac{\int_\Gamma \frac{\partial U_m^*}{\partial n} ds}{\int_\Gamma ds} \to \frac{dU_m^*}{dy}\right|_{y=b} = \alpha_m \tag{29}$$

2.5. Laplace Transform Inversions

[25] Time values C_c (x, t) and C_m (x, $-$, t) in any of the forms $C_m = C_m$ (x, r, θ, t), $C_m = C_m$ (x, ξ, η, t), or $C_m = C_m$ (x, z, y, t) are found by Laplace transform inversions [e.g., *Carslaw and Jaeger*, 1959]:

$$\{C_c, C_m\} = \mathcal{L}^{-1}\{U_c, U_m\} = \frac{1}{2\pi i}\int_{\delta-i\infty}^{\delta+i\infty} e^{pt}\{U_c, U_m\}dp \quad (30)$$

where δ is a small constant but sufficiently large to ensure that all singularities in the complex p plane lie to the left of the integral. For finite length conduits it is possible to obtain slowly converging residue series in the conduit as demonstrated in parallel-plate fracture models [*Robinson and Sharp*, 1997; *Robinson et al.*, 1998], but not in the matrix, unless boundary conditions can be imposed at finite distances from the conduit. For infinite length conduits, inversion to analytical integrals in the real domain appears to be a difficult problem unless the parallel line sections prevail, as in the work of *Tang et al.* [1981] and *Sudicky and Frind* [1982], both works providing infinite integrals. However, there are available robust and accurate methods of numerical inversion of Laplace transforms using either direct evaluation of the integral in equation (30), resulting in accelerated Fourier series convergence methods [*deHoog et al.*, 1982; *Piessens and Huysmans*, 1984], or the Talbot-Green contour deformation approach [*Talbot*, 1979; *Robinson and Maul*, 1991]. Confirmation of the accuracy of the *Piessens and Huysmans* [1984] routine has been achieved by comparison with the parallel plate, residue series solution [*Robinson and Sharp*, 1997].

[26] The rapid Talbot-Green routine was employed for all inversions after very close agreement with the Piessens and Huysmans method (10–14 decimal place agreement) when applied to the circular section and parallel lines conduit problems for selected parameters.

[27] For steady state conditions, the algebra is essentially the same as the above, and use is made of the Laplace transform properties [e.g., *Carslaw and Jaeger*, 1959]:

$$C_c(x,\infty) = \{pU_c(x,p)\}_{p\to 0} \quad (31)$$

$$C_m(x,r,\theta,\infty) = \{pU_m(x,r,\theta,p)\}_{p\to 0} \quad (32)$$

[28] If there is no decay then λ can be set to zero in the above equations.

3. Simulations of Conservative Species Transport

[29] Concentration profiles were simulated for a range of likely field situations to demonstrate the differences between conventional parallel-plate models and the new circular- and elliptical-section conduit models. The various simulations also provide quantitative estimates of solute penetration distances along the conduit and into the aquitard under different flow regimes and traveltimes.

3.1. Simulation Parameters

[30] Input parameters were based upon real solute properties and a range of likely field conditions. In this paper, we present only the simulation results for the transport of a conservative species, that is, decay and sorption are ignored ($\lambda = 0$, $R_c = R_m = 1$). If decay and/or sorption were included then this would obviously enhance the retardation of solute along the conduit and through the aquitard. For simplicity, we assigned equal values for the effective diffusion coefficients and effective porosities of the conduit and aquitard for all simulations, i.e., $D_{ce} = D_m$ and $\phi_c = \phi_m$ (Table 1). These values correspond to experimental data for the conservative chloride ion in clay-rich till aquitard [*Hendry and Wassenaar*, 1999], which will also be used for the case study presented below. The choice of a suitable value for longitudinal dispersivity (α_L) is contentious in any contaminant transport study [*Fetter*, 1999]. Here we assigned a value of 1 m for the conduit assuming a transport scale of several hundreds to thousands of meters [*Gelhar et al.*, 1992]. A total of six transport scenarios were tested, consisting of three different groundwater velocities (ν) in the conduit and two different conduit radii/plate half-widths (Table 1).

Table 1. Summary of Input Parameters for Generic Model Simulations

Scenario	$\phi_c = \phi_m$	$D_{ce} = D_{me}$ (m^2 yr^{-1})	α_L (m)	b (m)	ν (m yr^{-1})
1	0.22	6.6×10^{-3}	1	0.1	1
2	0.22	6.6×10^{-3}	1	0.1	100
3	0.22	6.6×10^{-3}	1	0.1	1000
4	0.22	6.6×10^{-3}	1	1	1
5	0.22	6.6×10^{-3}	1	1	100
6	0.22	6.6×10^{-3}	1	1	1000

3.2. Circular-Section Conduits Versus Parallel Plates

[31] A comparison between the parallel-plate solution of *Tang et al.* [1981], with additional porosity between the plates, and our circular conduit solution is provided for model scenarios 2 and 5 (Table 1) in Figures 2a and 2b. The simulated concentration profiles in these two plots show that solute penetrates farther along the aquifer and into the aquitard for larger b values. They also show that the conduit solution always yields lower concentrations than the parallel-plate solution throughout the model domain, but that the difference between the two solutions decreases with increasing values of b.

[32] Figures 2c and 2d present the ratio of relative concentration determined by the circular conduit solution to relative concentration determined by the parallel-plate solution. The x axes in these plots represent what we define as the relative distance x/x_0, where x_0 is the average distance the solute mass would be expected to move along the aquifer in a specified time if there was no mechanical dispersion nor loss of solute by diffusion into the aquifer (i.e., $x_0 = vt$). Thus $x/x_0 = 1$ corresponds to the position $x = vt$. This graphical approach enables the comparison of concentrations determined by the two solutions for different b values. Comparing Figures 2c and 2d shows that an increase in b results in better agreement between the two solutions for both the aquifer and aquitard at both early and late time throughout the model domain. For the input parameters used in these simulations, the parallel-plate solution provides an

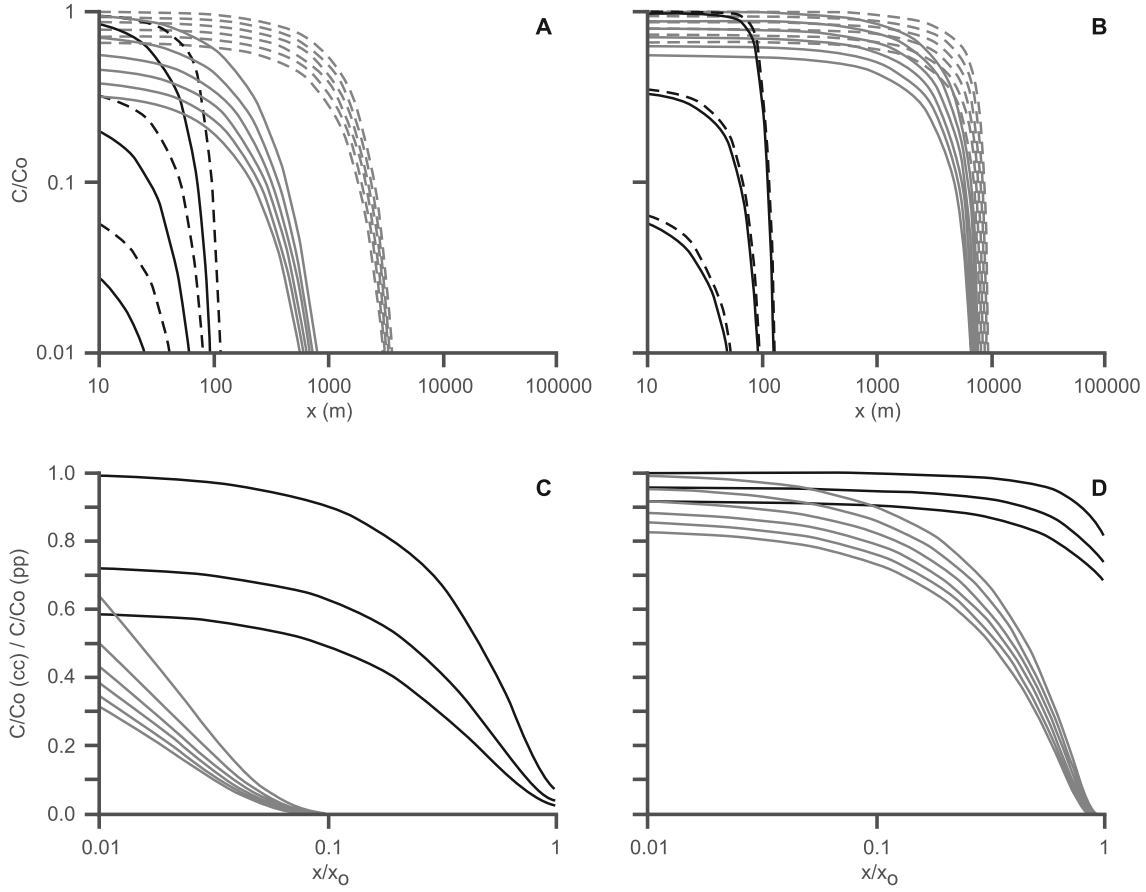

Figure 2. (a, b) Relative concentration profiles from the circular-conduit (solid lines) and parallel-plate (dashed lines) models for (Figure 2a) b = 0.1 m and (Figure 4b) b = 1.0 m after t = 1 yr (black lines) and t = 100 yr (grey lines). Average groundwater velocity v was 100 m yr^{-1} in both simulations. Curves represent various radial distances from the center of the conduit, with the right- and uppermost curve of each set representing the conduit-aquitard interface, and each successive curve representing 0.1-m increments into the aquitard. Increasing the value of b results in greater penetration of solute concentration along the conduit and into the aquitard, as well as closer agreement between the two models. (c, d) Ratio of relative concentration from the circular-conduit model to relative concentration from the parallel-plate model for (Figure 2c) b = 0.1 m and (Figure 2d) b = 1.0 m after t = 1 yr (black lines) and t = 100 yr (grey lines). The x axes represent relative distance x/x_0 where x_0 is the distance that solute would be expected to travel in the specified time if there was no retardation by chemical sorption, matrix diffusion, and decay. Increasing the value of b provides improved agreement between the two models at both early and late time throughout the expected transport domain.

adequate representation of concentration in both the circular conduit and aquitard at early time (i.e., t = 1 yr) for any value of $b \geq 1$ m. However, at a later time (t = 100 yr), increasing the value of b by a factor of 10 only provides reasonable agreement between the two solutions within the first 10% of the model domain (i.e., $x/x_0 < 0.1$). As $x/x_0 \rightarrow 1$, the parallel-plate solution yields concentrations for both the conduit and aquitard that are 10–1000 times greater than the circular conduit solution.

[33] To demonstrate the effects of increasing groundwater flow velocity on the concentration profiles using the parallel-plate and circular conduit approaches, we present solutions to scenarios 3 and 6 (Table 1) in Figures 3a–3d. The only difference between these plots and those shown in Figures 2a–2d is that the average groundwater velocity was increased from 100 to 1000 m/yr. Besides an increased scale in the x direction, the concentration profiles in Figures 3a and 3b are essentially the same as those in Figures 2a and 2b which suggest that groundwater velocity alone has little impact on the shape of the concentration profiles and the difference between the parallel-plate and circular conduit solutions. This can be further visualized in Figures 3c and 3d where the only major differences from Figures 2c and 2d are in the early time profiles in the second half of the expected transport domain (i.e., $x/x_0 > 0.5$).

3.3. Comparisons With Elliptical Cross Sections

[34] A series of simulations were run with scenario 2 for the Laplace transform inversion of the solutions for an elliptical cross-sectional conduit given in section 2.4.2. Some of the results are depicted in Figure 4 for t = 100 yrs and, for benchmarking purposes, corresponding numerical values in Tables 2 and 3. With selected aspect ratios of a/b = 1.25, 2.5, 5.0, 10.0, it is clear that the circular

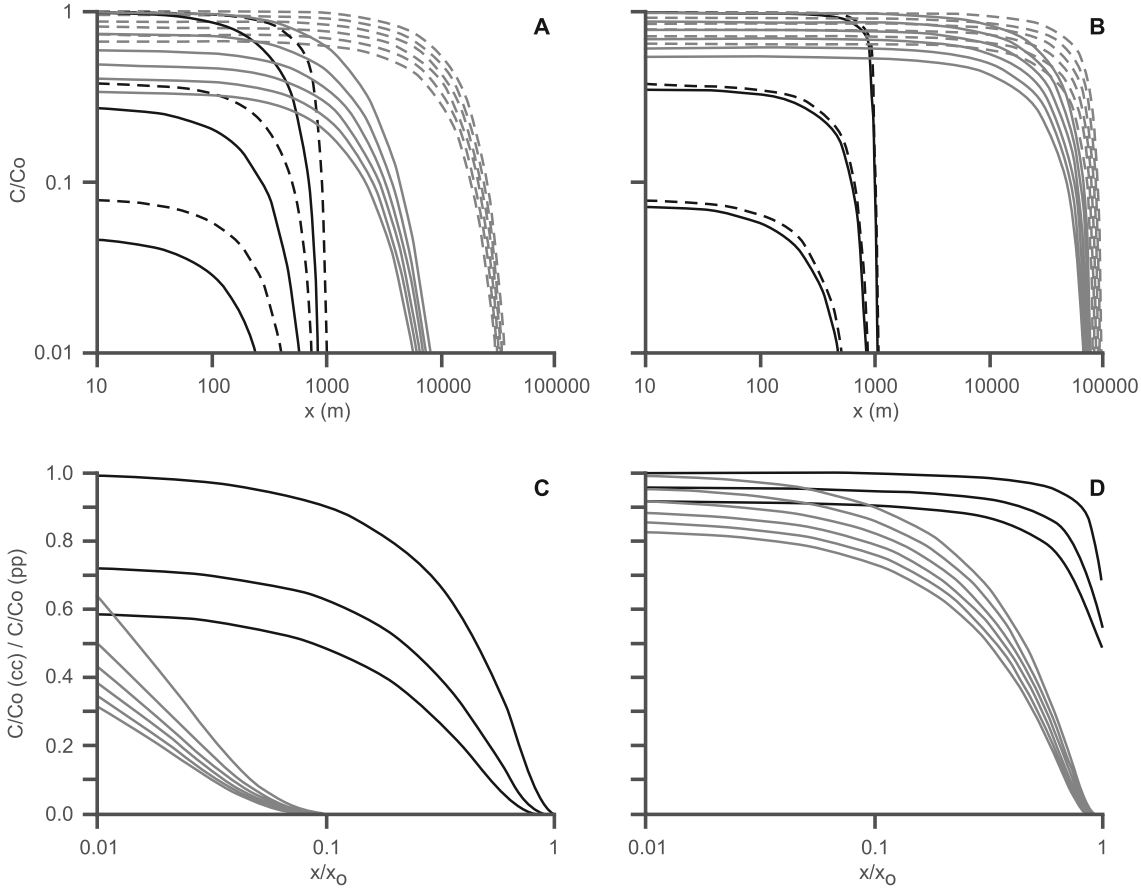

Figure 3. (a, b) Relative concentration profiles and (c, d) ratios of relative concentrations from the two model approaches, as per Figures 2a–2d, except average groundwater velocity v is 1000 m yr^{-1} (cf. 100 m yr^{-1}). Increasing the value of v causes solute to penetrate farther along the conduit and into the aquitard over the same time period. However, the difference between the circular-conduit and parallel-plate solutions tends to increase at early time (i.e., t = 1 yr) particularly toward the end of the expected transport domain.

section and parallel lines provide the expected limits to these results. The curves of Figure 4a are axial values of C_c/C_0 within and on the surface of the conduits. Those in Figure 4b show radial relative concentrations, C_m/C_0, from the surface at b = 0.1 m outwards into the aquitard at an axial position of x = 50 m. For emphasis, the constant concentrations of C_c/C_0 within the conduit are also shown. To show the effect of variations of radial concentrations for different values of θ, a value of a/b = 5 is chosen and results are shown in Figure 4c. The spread of values is not large, and the form is typical of other a/b ratios. All the curves for θ between 20°–90° are almost coincident implying that the normal derivatives of C_m are nearly constant along most of the perimeter of this ellipse, which lies close to the long boundary of a bounding rectangle.

[35] In order to perform the calculations, the series expressions of equation (23) are truncated with the number of terms required to give the accuracy shown in Tables 2 and 3 being {2, 5, 11, 23} corresponding to a/b = {1.25, 2.5, 5.0, 10.0}.

[36] To verify the calculations involved with the Mathieu functions, an alternative series solution was used for comparison. This involved adopting a polar coordinate series solution of the modified Helmholtz equation (13) as $U_m = \sum_{n=0}^{\infty} B_{2n} K_{2n}(\alpha_m r) \cos(2n\theta)$, where K_{2n} ( ) are modified Bessel functions of the second kind. Coefficients B_{2n} were determined from the boundary condition $U_m = U_c$ using confirmatory boundary methods of least squares minimization and boundary collocation. Up to aspect ratios of 2–2.5, agreement between the Mathieu function series and polar series was at least six decimal places. Beyond these ratios, severe numerical round off problems occurred with the polar series.

3.4. Effects of Velocity and Radius on Solute Penetration From a Circular Conduit

[37] The six simulation scenarios presented in Table 1 were used to demonstrate the sensitivity of the circular-section conduit model to different conduit radii and average groundwater flow velocities. Selected results from these simulations were presented earlier for comparison with the parallel-plate model. However, a more complete set of results for all six simulations is provided in Figures 5a–5f, enabling direct comparison of the solute concentration distributions for different values of b and v. Each plot contains three sets of curves representing short (1 yr), intermediate (10 yr), and long (100 yr) timescales of contaminant transport. The choice of these timescales was considered appropriate for typical

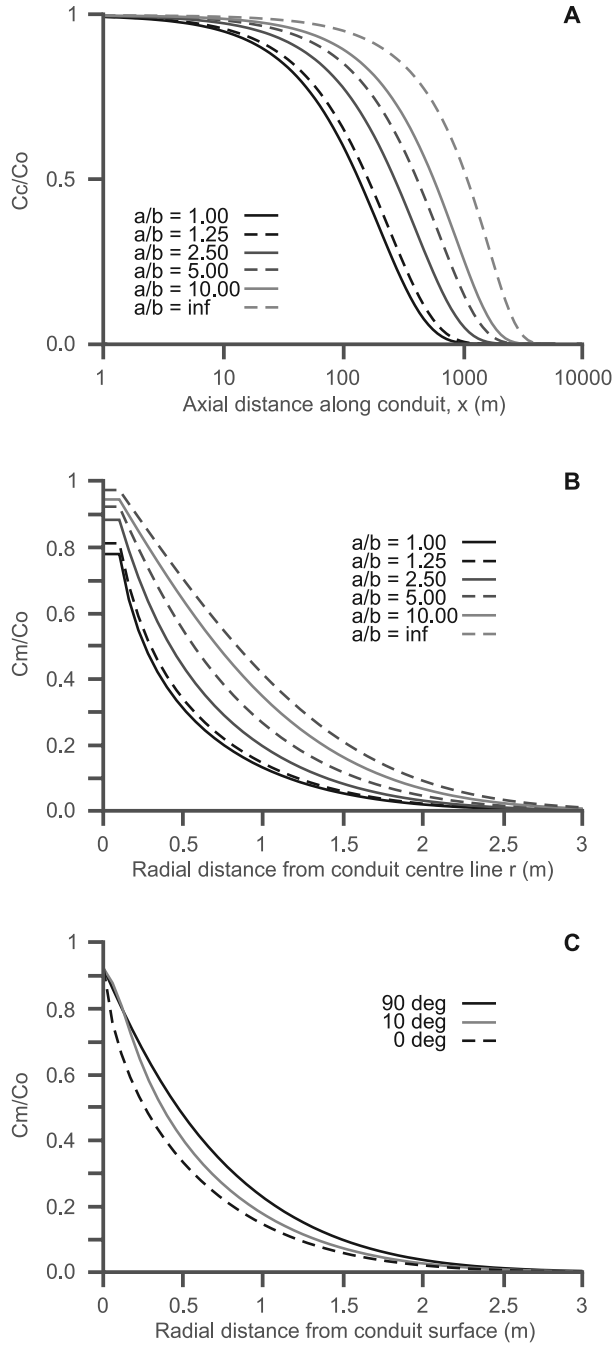

Figure 4. Relative concentration profiles for regular elliptical conduit cross-sections with aspect ratios a/b = 1.0 (circle), 1.25, 2.5, 5.0, 10.0, ∞ (parallel lines) determined for simulation input scenario 2 (Table 1) at t = 100 yrs. In Figure 4a, concentrations correspond to axial values along the conduits and at their surfaces. In Figure 4b, radial values of relative concentration within the aquitard are displayed for x = 50 m. Graphs in Figure 4c are representative of variations in concentrations around the perimeter of an ellipse of a/b = 5 with $\theta = 0°$, 10°, and 90°. Values of θ from 20°–90° graphically are close to coincidental.

investigations involving anthropogenic contamination of groundwater. (Longer-term simulation results are presented for natural contaminants in the case study below.) The curves within each set in Figures 5a–5f represent various radial distances r from the centre of the conduit, with the shortest distance (uppermost curve) representing the boundary between the conduit and the aquitard. The values of r for the b = 0.1-m simulations (Figures 5a, 5c, 5e) increase incrementally by 0.1 m; however, this scale is obviously inappropriate for the b = 1-m simulations, so the r increment in these cases is 0.5 m (Figures 5b, 5d, 5f).

Table 2. Axial C_c/C_0 Values Corresponding to Figure 4a at t = 100 yrs for Elliptical Sections

x \ a/b	1.0	1.25	2.5	5.0	10.0	∞
1	0.99515	0.99595	0.99761	0.99848	0.99895	0.99954
5	0.97595	0.97991	0.98809	0.99244	0.99475	0.99771
10	0.95243	0.96019	0.97629	0.98492	0.98953	0.99541
50	0.78206	0.81484	0.88621	0.92633	0.94830	0.97703
100	0.60835	0.66123	0.78373	0.85691	0.89827	0.95396
500	0.06730	0.10714	0.27119	0.43621	0.55750	0.76825
1000	0.00264	0.00750	0.05831	0.16204	0.27102	0.54494
2000	0.00000	0.00001	0.00117	0.01205	0.03706	0.19936
3000	0.00000	0.00000	0.00001	0.00029	0.00181	0.03979

[38] The results presented in Figure 5 suggest that, for a larger conduit radius, the solute will penetrate farther along the conduit and deeper into the aquitard in a given time. Increasing the average groundwater flow velocity will also lead to farther penetration along the conduit. However, with increasing flow velocity, the magnitudes of the concentration profiles at various radial distances into the aquitard remain essentially unchanged in the first 10% of the expected transport domain. For example, Figures 5d and 5f show concentration profiles at 0.5-m radial increments for cases of v = 100 m/yr and v = 1000 m/yr, respectively (b = 1 m). In comparing the long-term solutions, we see that the concentration profiles are the same in both plots for r = 1, 1.5, 2, 2.5, and 3 m in the first 10% of the expected transport domain (i.e., the first 1000 m and 10,000 m for Figures 5d and 5f, respectively). Therefore we suggest that varying the groundwater velocity in the conduit will only affect depths of solute penetration into the aquitard for relative distances $z/z_0 > 0.1$.

3.5. Nondimensional Results

[39] In addition to the dimensional results presented above, it is useful to have nondimensional results for wider application. To do this the cross-sectional length parameter w, as a ratio of conduit cross-sectional area to conduit perimeter defined by equation (9), is used. Multiplying both sides of differential equations (2) and (3) by w^2 produces the

Table 3. Radial C_m/C_0 Values Corresponding to Figure 4b at t = 100 yrs for Elliptical Sections

r \ a/b	1.0	1.25	2.5	5.0	10.0	∞
0–0.1	0.78206	0.81484	0.88621	0.92633	0.94830	0.97703
0.25	0.51191	0.55277	0.67287	0.76884	0.82830	0.87313
0.5	0.31170	0.34054	0.43958	0.54995	0.64174	0.70556
1.0	0.13138	0.14506	0.19594	0.26625	0.34725	0.41559
1.5	0.05337	0.05942	0.08272	0.11762	0.16403	0.21116
2.0	0.01950	0.02188	0.03127	0.04600	0.06713	0.09167
2.5	0.00264	0.00705	0.01032	0.01562	0.02357	0.03376
3.0	0.00172	0.00196	0.00293	0.00454	0.00704	0.01049
4.0	0.00008	0.00009	0.00015	0.00023	0.00038	0.00060

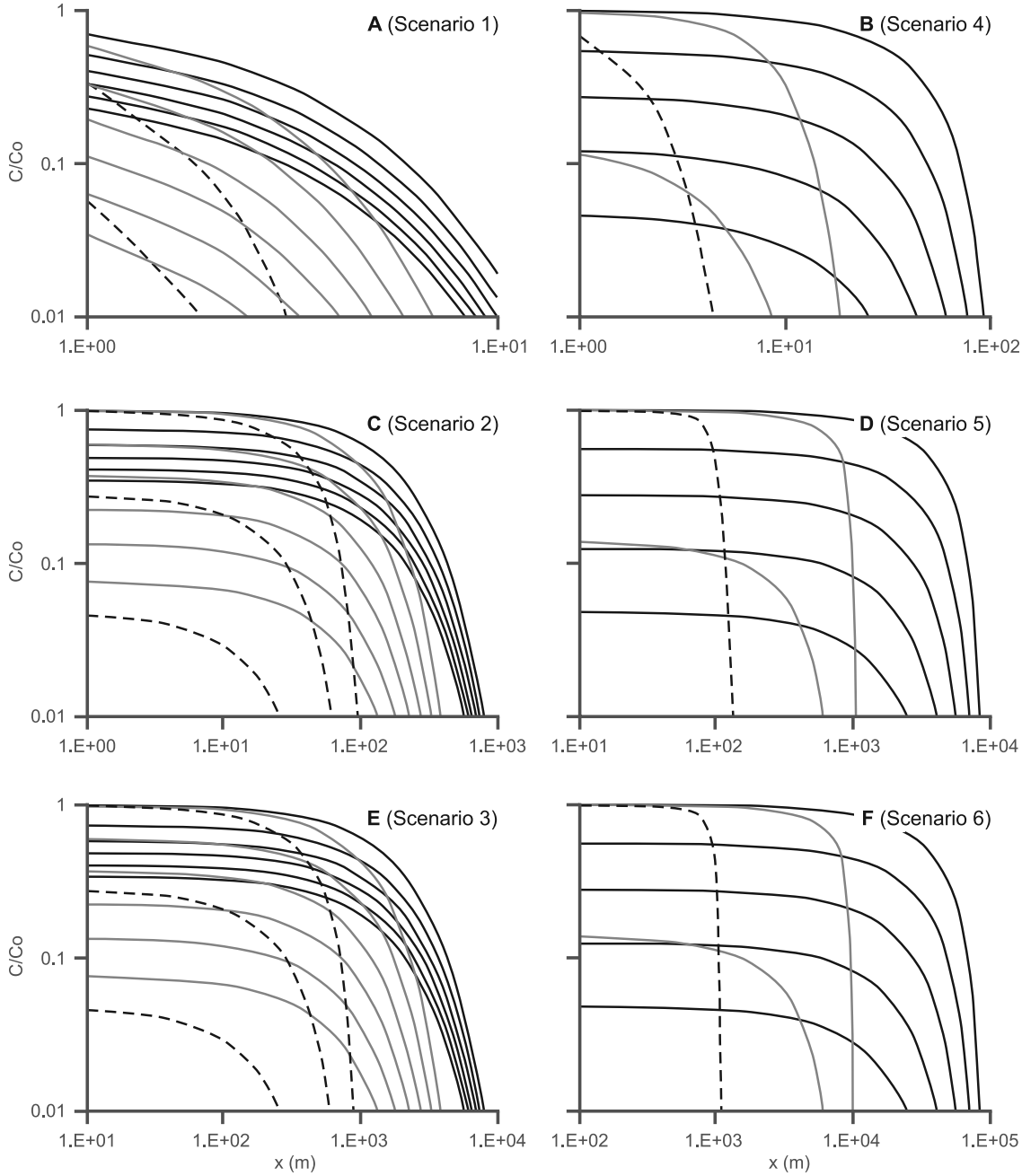

Figure 5. (a–f) Relative concentration profiles for simulation scenarios 1–6 (Table 1) determined using the circular-conduit model. Results are presented for three different times as follows: $t = 1$ yr (dashed lines), $t = 10$ yr (grey lines), and $t = 100$ yr (black lines). Curves represent various radial distances from the center of the conduit, with the right- and uppermost curve of each set representing the conduit-aquitard interface, and each successive curve representing incremental distances into the aquitard (0.1 m for scenarios 1–3, 0.5 m for scenarios 4–6). Increasing v by an order of magnitude results in a near proportional increase in the horizontal distribution of solute in the conduit and aquitard, but very minor changes in concentration distribution at radial distances away from the conduit. Increasing b by an order of magnitude results in an almost proportional increase in horizontal migration along the conduit, as well as much higher concentrations in the surrounding aquitard.

nondimensional equations (except for C_c and C_m, which can be scaled by C_0)

$$\frac{\partial^2 C_c}{\partial x^{*2}} - \beta_1 \frac{\partial C_c}{\partial x^*} - \beta_2 \lambda^* C_c + \beta_3 F_m = \beta_2 \frac{\partial C_c}{\partial t^*} \tag{33}$$

$$\nabla^{*2} C_m - \lambda^* C_m = \frac{\partial C_m}{\partial t^*} \tag{34}$$

The nondimensional quantities are defined as follows:

$$\beta_1 = \frac{wv}{D_c}, \qquad \beta_2 = \frac{D_m R_c}{D_c R_m}, \qquad \beta_3 = \frac{D_m \phi_m}{D_c \phi_c}$$

$$\lambda^* = \frac{w^2 R_m}{D_m}\lambda, \; t^* = \frac{D_m}{w^2 R_m} t \tag{35}$$

$$x^* = \frac{x}{w}, \; y^* = \frac{y}{w}, \; z^* = \frac{z}{w}, \nabla^{*2} = w^2 \nabla^2$$

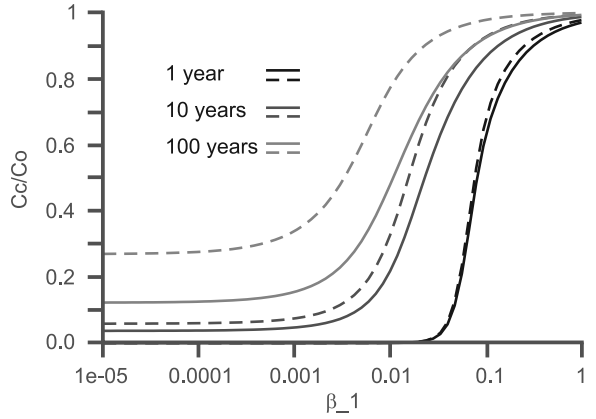

Figure 6. Nondimensional results. Axial concentrations are shown for variations in β_1 holding β_2 and β_3 constant (parallel plates, dashed; circular conduits, solid). Base case values are formed from scenario 2 with $w = 0.1$ m, $x = 50$ m or $x^* = 500$, and $\beta_1 = 0.1$, $\beta_2 = 6.6 \times 10^{-5}$, and $\beta_3 = 9.9 \times 10^{-6}$. Three sets of curves are given for $t = \{1, 10, 100\}$ yrs or $t^* = \{0.66, 6.6, 66\}$.

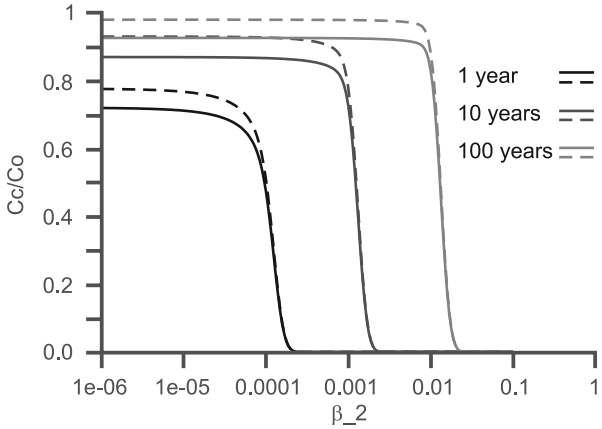

Figure 7. Nondimensional results. Axial concentrations (parallel plates, dashed; circular conduits, solid) are shown for variations in β_2 holding β_3 and β_1 at base case values with $w = 0.1$ m, $x = 50$ m or $x^* = 500$, and $t = \{1, 10, 100\}$ yrs or $t^* = \{0.66, 6.6, 66\}$.

The matrix flux factor F_m is defined by

$$F_m = w \frac{\int_\Gamma \frac{\partial C_m}{\partial n} ds}{\int_\Gamma ds} \tag{36}$$

The procedure for the Laplace transform solution is much the same as for the dimensional equation system.

[40] With quantities C_c/C_0, C_m/C_0, x^*, y^*, z^*, β_1, β_2, β_3, λ^*, t^* to be evaluated, there are too many combinations to present all possibilities here, and, as in the dimensional case, a restricted set is examined. Scenario 2 is adopted as a base case, and attention is given to variations in β_1, β_2, and β_3 with discrete values of x^*, y^*, z^*, ($\lambda^* = 0$), and t^*. The base case values provide $w = 0.1$ for parallel plates and $\beta_1 = 0.1$, $\beta_2 = 6.6 \times 10^{-5}$ and $\beta_3 = 9.9 \times 10^{-6}$. The circular conduit radius is doubled in order to maintain the same w. By holding β_2 and β_3 constant and varying β_1 it can be seen from Figure 6 for circular sections and parallel plates that at a particular value of $x = 50$ m or $x^* = 500$ and times $t = \{1, 10, 100\}$ yrs or $t^* = \{0.66, 6.6, 66\}$, the magnitude of the axial concentration, C_c/C_0, increases as β_1 increases. One way of interpreting this is to increase ν in $\beta_1 = wv/D_c$ and hold w and D_c constant. A higher velocity will increase downstream concentrations at particular positions as would be required and already shown in Figures 3a and 3b. The increased spread between circular section and parallel-plate results for increasing time is also consistent with that shown in Figures 2a and 2b. In similar fashion of varying β_2 only as in Figure 7 and β_3 only as in Figure 8, a decrease in axial concentration for the same axial position and time conditions for increasing $\beta_2 = D_m R_c/D_c R_m$ and $\beta_3 = D_m\phi_m/D_c\phi_c$ can be interpreted as increases in the retardation ratio R_c/R_m and porosity ratio ϕ_m/ϕ_c, respectively.

4. Case Study: Southern Saskatchewan, Canada

4.1. Study Site

[41] The King site is located approximately 5 km northeast of the township of Birsay (latitude 51.096275, longitude 106.97813) in southern Saskatchewan, Canada. The landscape surrounding the site is typical of the gently undulating prairies that dominate the western glaciated plains of North America. Near-surface geology consists of approximately 80 m of clay-rich, carbonaceous Battleford Till overlying an additional 77 m of plastic, marine clay (Snakebite Member) [*Christiansen*, 1986; *Shaw and Hendry*, 1998]. Hydrogeological and hydrochemical studies conducted at the site over the last 10 years have determined that the K of the unoxidized and unfractured till is extremely low ($K < 10^{-10}$ m s^{-1}) and that solute transport is dominated by diffusion rather than advection [e.g., *Harrington and Hendry*, 2005; *Hendry and Wassenaar*, 1999, 2000; *Hendry et al.*, 2000].

4.2. Evidence of Physical Heterogeneity

[42] The Battleford till was previously considered to be homogeneous in terms of its mineralogy and grain-size distribution [*Shaw*, 1997; *Yan et al.*, 2001]. However, the

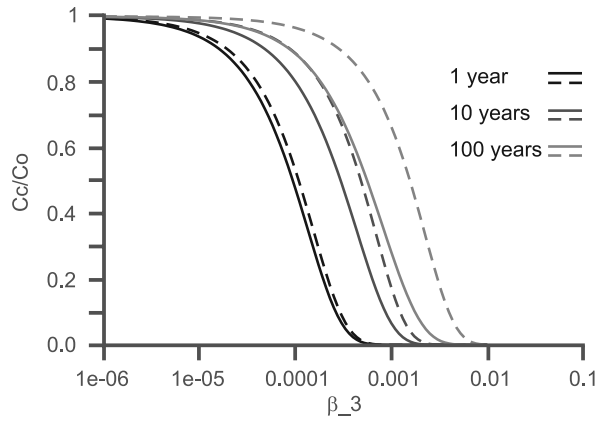

Figure 8. Nondimensional results. Axial concentrations (parallel plates, dashed; circular conduits, solid) are shown for variations in β_3 holding β_1 and β_2 at base case values with $w = 0.1$ m, $x = 50$ m or $x^* = 500$, and $t = \{1, 10, 100\}$ yrs or $t^* = \{0.66, 6.6, 66\}$.

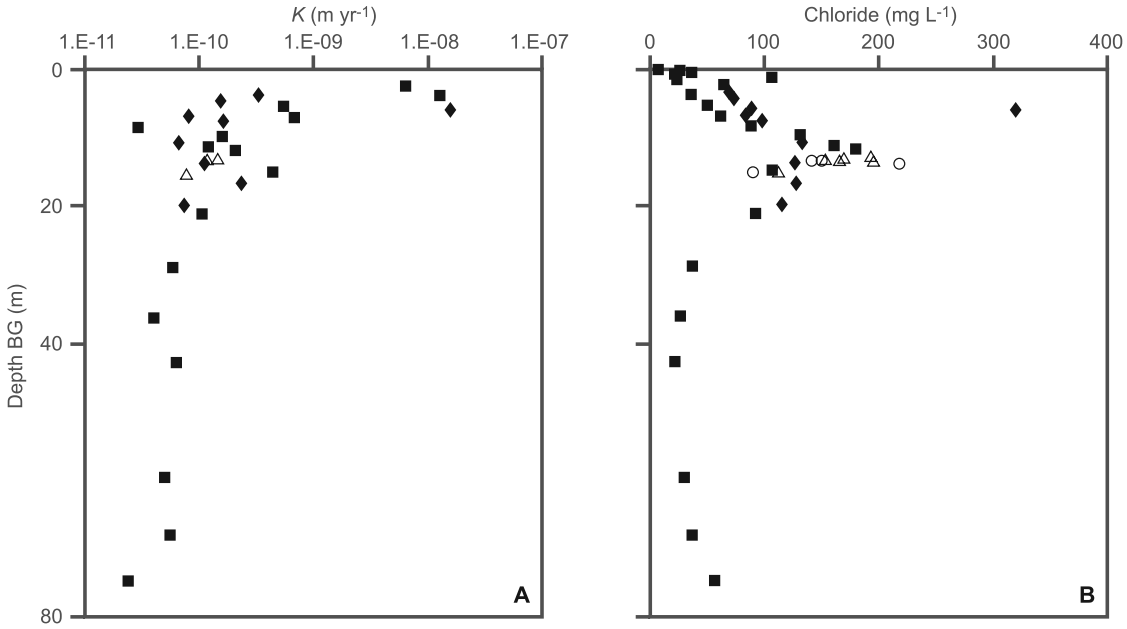

Figure 9. (a) Hydraulic conductivity estimated from water-level recovery data, and (b) pore water chloride concentrations, both versus depth below ground level. Symbols reflect different series of piezometers (solid squares, B-series; open triangles, BD-series; solid diamonds, BJ-series; open circles, BG-series). Error bars represent screen intervals. Both the K and Cl^- profiles exhibit local peaks at between 10–15 m below ground, likely reflecting the presence of a sand deposit at this depth.

extensive drilling and coring programs, hydraulic testing, and hydrochemical sampling undertaken at the King site in recent years have provided corroborative evidence for a sand deposit located approximately 10–15 m BG.

4.2.1. Drilling Observations and Hydraulic Measurements

[43] Four phases of rotary auger drilling were carried out at the site over the last 10 years, allowing the installation of four series of piezometers (B, BD, BJ, and BG series) with each series designed to suit specific experimental purposes. Several boreholes in each series were cored at the time of drilling for subsequent mineralogical and pore water chemical analyses. Many of the cores recovered from 10–15 m BG contained a medium- to coarse-grained sand layer within the fine-grained, clayey till matrix. For example, *Shaw* [1997] noted that sand streaks are present in most B-series cores collected between 11–15 m. Thin sand layers were also observed in cores from the BD-series and BJ-series wells at this depth. Most recently, six BG-series piezometers were installed at the site after direct-push electrical conductivity (D-P EC) logging during May–June 2004 revealed a 0.8–4.5-m-thick sand deposit in four locations [*Harrington and Hendry*, 2005]. Boreholes were drilled and cored at these four sites to confirm that the EC anomalies observed between 9.4–15.9 m BG were, in fact, sand and to provide sediment samples for grain-size analysis. The K of the sand extracted from the cores was estimated from grain-size distribution curves using the method of *Hazen* [1892] and ranged between 1.4×10^{-2} to 2.3×10^{-2} ms^{-1} (uniformity coefficients were ~3.3). Groundwater samples were also taken from the BG-series piezometers for major ion and radiocarbon analysis (see below).

[44] Water-level recovery data from 20 B-series piezometers were used by *Shaw* [1997] to calculate values of K for each piezometer using the method of *Hvorslev* [1951]. We reevaluated Shaw's original K values using more extensive water-level data and produced a similar depth profile (Figure 9a). The vertical profile indicates that K is greatest, albeit highly variable, in the top 4–8 m BG which is consistent with the fractured and highly oxidized nature of the till in this zone [*Shaw and Hendry*, 1998]. The till becomes unoxidized below 6–8 m depth due to an absence of fractures, and accordingly, the value of K between 8–10 m BG is relatively low compared with shallower depths. Between 10–15 m BG the value of K increases toward a local peak value $\sim 5 \times 10^{-10}$ ms^{-1} before decreasing to values $<1 \times 10^{-10}$ ms^{-1} throughout the remaining till. The localized peak in K at around 12–15 m BG is presumed to reflect the influence of the more permeable sand deposit.

4.2.2. Pore Water Chloride Distribution

[45] Several hundred hydrochemical analyses of water samples collected from more than 50 piezometers have shown the till water is Na^+-SO_4^{2-} dominated. The mechanisms responsible for the chemical evolution from rainwater to this Na^+-SO_4^{2-} type are primarily oxidation of reduced sulfur compounds (for example, FeS_2), dissolution of gypsum, and cation exchange of Ca^{2+} for Na^+ on clay-mineral surfaces [*Hendry and Wassenaar*, 2000]. These reactions occur in the shallow, oxidized zone of the till, resulting in an accumulation of dissolved salts that are ultimately transported to deeper, fresher parts of the till by diffusion. Hence vertical profiles of most major ion species and some isotopic species (for example, δ^2H, ^{14}C, ^{13}C) exhibit a classic diffusion-curve shape [*Hendry and Wassenaar*, 1999, 2000; *Wassenaar and Hendry*, 2000]. The only major

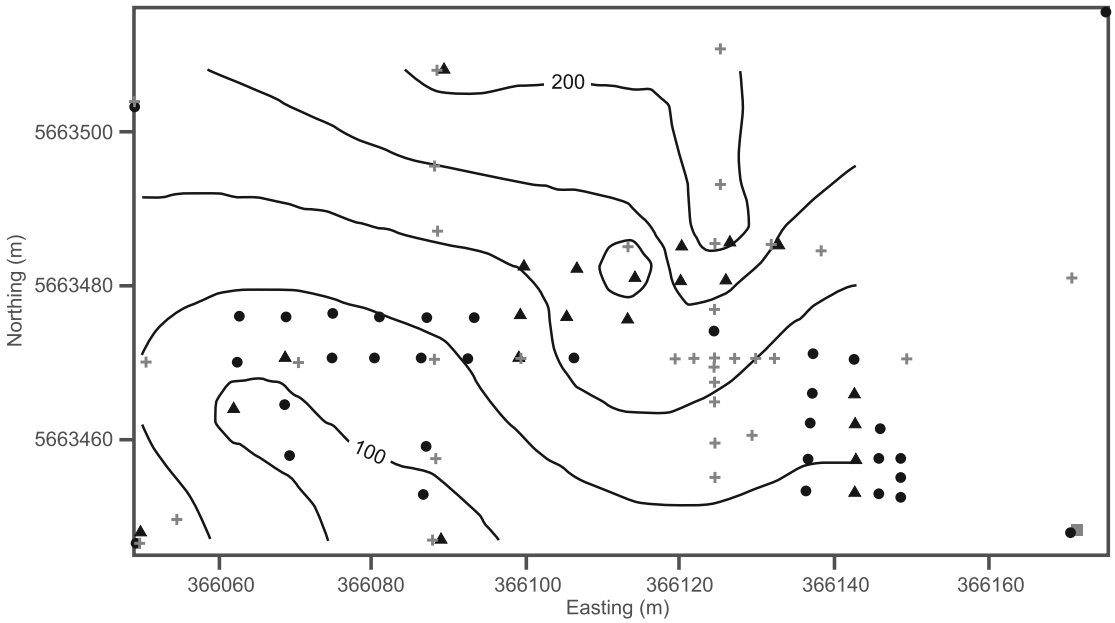

Figure 10. Map showing the locations of all piezometers (circles/triangles) and direct-push EC logs (crosses) at the King site. Contour lines reflect pore water Cl^- concentration (CI = 25 mg L^{-1}) in piezometers constructed between 10–20 m below ground (triangles). Circles mark the locations of piezometers screened either above or below this zone. The zone of high Cl^- coincides with locations where a sand deposit was observed in drill cuttings, cores, and Direct Push EC logs [*Harrington and Hendry*, 2006].

ions that exhibit atypical and unexplainable vertical profiles through till are the halides, chloride, and bromide [*Hendry et al.*, 2000]. Figure 9b shows the vertical distribution of pore water Cl^- concentration from all four series of piezometers. A similar trend (not shown) exists for Br^- concentration [*Hendry et al.*, 2000]. The most striking feature of the Cl^- profile in Figure 9b is the peak in concentration between 10–20 m BG. *Hendry et al.* [2000] suggested that this peak reflects the impact of the sand deposit. They used one-dimensional advection-diffusion models to estimate a timescale of 5 kyr for the development of the diffusion profile below the peak. However, even with the aid of chlorine isotope techniques (^{36}Cl, $\delta^{37}Cl$), they were unable to determine the source and evolution of the Cl^- peak.

[46] We investigated several possible mechanisms for the origin of the Cl^- peak, including (1) salinity stratification in connate water at the time of till deposition, (2) evaporative concentration of rainfall at the ground surface during a more arid period than currently exists, and (3) contamination somewhere off-site and transport along the sand layers. One-dimensional advection-diffusion models similar to those applied by *Hendry et al.* [2000] were used to test the first two of these possible mechanisms. For the case where the Cl^- peak commenced at the time of till deposition, we ran a series of numerical model simulations with each having a different initial Cl^- concentration in the peak zone. Regardless of the initial concentration, we found that after a timescale commensurate with the age of the till (15–30 kyr [*Christiansen*, 1971; *Hendry and Wassenaar*, 1999; *Hendry et al.*, 2000; *Wassenaar and Hendry*, 2000]) the simulated Cl^- peaks (not shown) were much broader than the observed profile shown in Figure 9b. Therefore it is highly unlikely that the Cl^- peak is a remnant feature from till deposition; this finding is consistent with the assumption that depositional water chemistries were homogeneous throughout the till [*Hendry and Wassenaar*, 2000].

[47] Pore water δ^2H and ^{14}C-DOC (dissolved organic carbon) data suggest that a warm altithermal period may have occurred 10–12 kyr BP [*Hendry and Wassenaar*, 1999, 2005]. We used both an analytical solution and a simple numerical model to simulate the movement of a high-Cl^- source from the water table commencing 10 kyr BP. This modeling resulted in the development of broad, subdued Cl^- peaks similar to those obtained for the depositional Cl^- mechanism (above). To displace the Cl^- peak from the water table (1–3 m BG) to its current position (11–13 m BG) in the 10 kyr timescale also required pore water velocities up to an order of magnitude greater than the 0.8 m per 10 kyr used in previous modeling studies at the site [*Hendry and Wassenaar*, 1999; *Hendry et al.*, 2000]. Therefore it is unlikely that this mechanism is responsible for the current Cl^- peak.

[48] The only plausible hypothesis for the origin of the Cl^- peak is that it is associated with the sand deposit and is imported from somewhere off-site. Figure 10 shows a contour map of pore water Cl^- concentration in piezometers screened between 10–20 m BG. Also shown are the locations of all wells and D-P EC logs. The apparent encroachment of high Cl^- into the center of the site from the north is also consistent with locations where we observed sand in the BG-series boreholes [*Harrington and Hendry*, 2006].

[49] Sampling of the BG-series piezometers (the only piezometers completed in the sands) during 2004 confirmed earlier observations that niether of the major ions (except

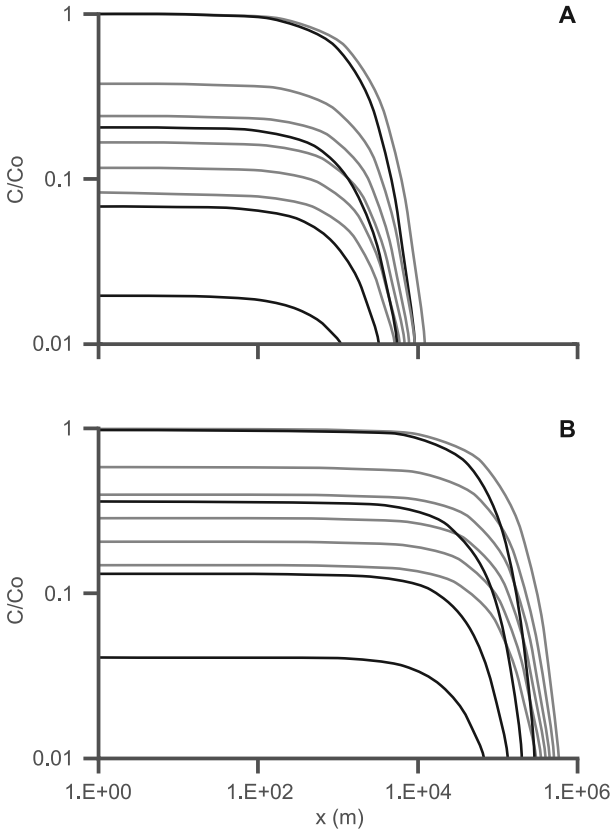

Figure 11. (a) Simulated relative concentration profiles for the King site application, with a sand conduit radius of 0.1 m and (b) 1 m. Curves represent output at two different times (1 kyr, black lines; 10 kyr, grey lines) and various radial distances from the conduit-aquitard interface; the right- and uppermost curves represent concentration at the interface, and each successive curve represents an incremental distance of 0.2 m (Figure 11a) and 2 m (Figure 11b) into the aquitard. These results show the source of high Cl^- may be as far away as 10^4–10^5 m (10–100 km) if it has persisted for the last 1–10 kyr. The results also demonstrate how evidence of high-Cl^- transport along the sand deposit can be observed up to 10 m into the aquitard.

Cl^-), carbon isotopes ($^{13}C/^{12}C$ and ^{14}C), nor stable isotopes of water ($^2H/^1H$ and $^{18}O/^{16}O$) differ from the general depth trends in the aquitard. The fact that no other chemical or isotopic species exhibits peaks at the same depth suggests that the source water associated with the Cl^- peak must undergo the same geochemical interactions as all other till pore water. To further investigate the processes associated with Cl^- transport along sand deposit, we utilized the solutions for radial diffusion from conduits presented earlier.

4.3. Application of Conduit Diffusion Models

[50] The various forms of sand deposit observed at the site range in thickness from 1×10^{-2} m (as streaks) to ~4 m (as channels). The discontinuity of these features between adjacent boreholes in an E-W orientation means they have limited lateral extent across the site and should be treated as conduits rather than parallel plates for contaminant transport purposes. However, to be able to import Cl^- to the site from the north implies that the conduits must be more laterally extensive in the N-S direction. We used the circular conduit solution to model Cl^- transport through the sand because we could not adequately characterize the geometry of the deposit for applying the elliptical cross-section model. Nevertheless, as observed in section 3.3, the circular conduit solutions provide the maximum loss of solute by radial diffusion into the matrix.

[51] On the basis of the range of K values determined for the sand deposit (1.4×10^{-2} to 2.3×10^{-2} ms^{-1}) and the low horizontal hydraulic gradient across the site (~0.0005), we estimated an average groundwater velocity of 1000 myr^{-1} for Cl^- transport through the conduit. To reflect the range of observed conduit radii and the likely timescales for Cl^- transport, we ran four model simulations comprising two different values for b (0.1 and 1 m) and two simulation times (1 and 10 kyr). Thus the range of input parameters, including porosities and effective diffusion coefficients, correspond to the generic scenarios 3 and 6 (Table 1).

[52] Results for the King site application are presented in Figures 11a and 11b with each plot containing model output at various radial distances up to 10 m from the edge of the conduit for the two simulation times. Because the only difference between the two plots is the value of b, the different results are consistent with the observations we made earlier for the generic simulations (cf. Figures 5e and 5f). Figure 11 provides several useful insights to the origin and evolution of the Cl^- peak at the site. First, the curves representing Cl^- concentration in the conduit (i.e., r = 0.1 m and r = 1 m in Figure 11a and 11b, respectively) suggest that if the source of high Cl^- commenced 1–10 kyr BP then it might be as far away as 10–100 km. This distance is extreme and most likely impossible to achieve given the changes in landscape and geology over this scale. Nevertheless, the model demonstrates that the source of high Cl^- may be far from the site. The concentration profiles shown in Figure 11 for various radial distances indicate that even if the source is only 1–10 km off-site then we should be able to observe evidence of the Cl^- pulse in the till at distances of 5–10 m from the perimeter of the conduit. This explains why we see relatively high Cl^- concentrations in the 10–20 m BG zone several meters away from the nearest sand observation. Finally, by selecting a suitable conduit concentration curve from either Figures 11a or 11b, one can estimate a value of C/C_0 at any distance x to calculate the Cl^- concentration of the source. Because we are not confident in suggesting that the source is 10–100 km away, we provide an example assuming the source is only 1000 m away. In this case, the value of C/C_0 in the conduit at x = 1000 m is 0.62–0.69 after 1–10 kyr for b = 0.1 m (Figure 11a) and 0.99 after 1–10 kyr for b = 1 m (Figure 11b). Therefore the Cl^- concentration at the source, C_0 is 152–242 mg/L (1.01–1.62 × C) if we assume an average peak Cl^- concentration of 150 mg/L at x=1000 m (Figure 9b). A cursory review of any possible high-Cl^- features in the surrounding landscape has so far failed to reveal the source, but we now have an understanding of how and over what scales the Cl^- peak may have evolved.

5. Concluding Remarks

[53] Sand deposits are common in many aquitards. These features can provide preferential pathways for solutes,

including contaminants, to advect through what is otherwise a diffusion-dominated environment. We developed and applied mathematical models to assess the effects of sand deposits (porous conduits) on solute transport in aquitards. The model solutions account for advective transport of reactive solutes through porous conduits of either circular or elliptical cross sections, with simultaneous loss of solute mass by radial diffusion into the surrounding aquitard.

[54] A comparison of simulation results for solute transport within parallel planar aquifers, circular-section conduits, and various elliptical-section conduits revealed significant differences in predicted concentration, both along the aquifer/conduit axis and at various radial distances into the matrix. The results suggest that using a conventional parallel-plate approach to predict solute transport within and around permeable conduits in an aquitard will yield significantly lower concentrations than those predicted using a circular conduit approach, or even an elliptical conduit of aspect ratio $a/b < 10$.

[55] Numerous simulations were performed to investigate the effects of different conduit radii (circular-section conduits) and groundwater velocities under typical field conditions. They showed that increasing the average groundwater velocity by an order of magnitude (from 100 to 1000 m yr^{-1}) yielded an almost proportional increase in the distance of horizontal solute penetration along the conduit. In contrast, increasing the conduit radius resulted in disproportionate increases in both conduit and aquitard concentrations throughout the model domain.

[56] A circular-sectioned conduit model was used to provide insight into the source of an anomalously high-Cl^- peak observed 10–15 m BG in clay-rich till at the King research site in southern Saskatchewan, Canada. Physical characteristics, chemical and isotopic trends, and model results indicate the source of high Cl^- is most likely associated with a sand deposit at the same depth. Model results further showed that the Cl^- could come from as far away as 10–100 km. The results were also used to estimate a Cl^- concentration of 150–250 mg/L for the source assuming a transport distance of 1000 m. The simulations demonstrate how evidence of high-Cl^- transport along the sand deposit can be observed up to 10 m into the aquitard. We suggest that the presence of anomalous concentration data in aquitards, such as measured at the King site, could be caused by diffusion of solutes from permeable conduits. With models such as those we have presented, one can use the concentration data to help locate these conduits and provide insight into the source area for the solute and the length of time that the solute has migrated along the conduit.

[57] We expect that the model solutions presented in this study will be useful for predicting the transport behavior of anthropogenic contaminants in future aquitard studies. In addition, there are a number of other potential hydrogeological applications for these models that do not involve aquitards. These include solute transport within paleochannel aquifers, applied tracer tests in karst environments, radial diffusion of salts from pervious pipes, and tracer studies within partially cemented or closed fractures. Regardless of the application, the challenge will always be to define the geometry of the conduit and its flow conditions. Nevertheless, the generic and applied model solutions that we have presented demonstrate the importance of using a conduit approach instead of, or in addition to, the traditional parallel-plate models in many field situations.

Appendix A: Solution for the Matrix With an Elliptical Hole

[58] The modified Helmholtz equation (13), rewritten in elliptical coordinates for ∇^2 given in equation (22):

$$\frac{2}{h^2(\cosh 2\xi - \cos 2\eta)}\left(\frac{\partial^2}{\partial\xi^2}+\frac{\partial^2}{\partial\eta^2}\right)U_m - \alpha_m^2 U_m = 0 \qquad \text{(A1)}$$

is to be solved for $U_m = U_c$ on the boundary Γ of an elliptical hole in the matrix of infinite extent. α_m^2 is a complex quantity directly dependent on the Laplace transform variable p. Not only is the solution for U_m required outside the hole in the matrix, but it is necessary to find $\int_\Gamma \partial U_m/\partial n \, ds$ as a component of the conduit equation (8).

[59] With the bounding ellipse defined in Cartesian coordinates (z, y), $-a \le z \le a$, $-b \le y \le b$ and $a \ge b$, a transformation to elliptical coordinates (ξ, η), with the relationships $z = h \cosh\xi \cos\eta$, $y = h \sinh\xi \sin\eta$, produces ellipses with constant ξ values and orthogonal hyperbolae with constant η values. Their equations are $z^2/h^2 \cosh^2\xi + y^2/h^2 \sinh^2\xi = 1$ and $z^2/h^2 \cos^2\eta - y^2/h^2 \sin^2\eta = 1$. With $\xi = \xi_0$, corresponding to $z^2/a^2 + y^2/b^2 = 1$ on Γ, then $h^2 = a^2 - b^2$, and $\xi_0 = \cosh^{-1}(a/h)$, with particular values of η as $\eta = 0, \pi$ for $y = 0$, and $\eta = \pi/2, 3\pi/2$ for $y = \pm b$.

[60] When it is assumed that U_m can be expressed as the product of separated functions of ξ and η, i.e., $U_m = \psi(\xi)\phi(\eta)$, and then substituted in equation (A1), the two Mathieu ordinary differential equations are produced

$$\frac{\partial^2\psi}{\partial\xi^2} - (e + 2q\cosh 2\xi)\psi = 0 \qquad \text{(A2)}$$

$$\frac{\partial^2\phi}{\partial\eta^2} + (e - 2q\cos 2\eta)\phi = 0 \qquad \text{(A3)}$$

Here $q = \alpha_m^2 h^2/4$ and e represents one of an infinite number of separation constants; the calculation of which will be outlined below. There are solutions of equations (A2) and (A3) as $2m$th-order Mathieu functions $Fek_{2m}(\xi,-q)$ and $ce_{2m}(\eta,-q)$, both suited to the quadrant symmetry of behavior of the ellipses. The notation follows that of *McLachlan* [1947]. At large distances from the hole, $\xi \to \infty$ and $Fek_{2m}(\xi,-q) \to 0$ as required. $ce_{2m}(\eta,-q)$ displays bounded oscillatory behavior and $0 \le \eta \le 2\pi$.

[61] The general solution for equation (A1) can now be written as

$$U_m = \sum_{m=0}^{\infty} B_{2m} Fek_{2m}(\xi,-q) ce_{2m}(\eta,-q) \qquad \text{(A4)}$$

with coefficients B_{2m} to be determined.

[62] An appropriate representation for $ce_{2m}(\eta,-q)$ is [*McLachlan*, 1947, p. 21]

$$ce_{2m}(\eta,-q) = (-1)^m \sum_{r=0}^{\infty} (-1)^r A_{2r}^{(2m)} \cos 2r\eta \qquad \text{(A5)}$$

where the $A_{2r}^{(2m)}$ are coefficients associated with, and determined by, the infinite set of separation constants e_{2m}. The derivation process for $A_{2r}^{(2m)}$ and a suitable form of $Fek_{2m}(\xi, -q)$ will be given below.

[63] To solve for the boundary condition $U_m = U_c$ at $\xi = \xi_0$, the following identity is used [*McLachlan*, 1947, p. 209]

$$1 = 2\sum_{m=0}^{\infty}(-1)^m A_0^{(2m)} ce_{2m}(\eta, -q) \tag{A6}$$

[64] Multiplying both sides of this identity by U_c and setting $\xi = \xi_0$ in the expression (A4) for U_m leads directly to

$$B_{2m} = \frac{2(-1)^m A_0^{(2m)} U_c}{Fek_{2m}(\xi_0, -q)} \tag{A7}$$

so that the solution for U_m is given by

$$U_m = 2U_c \sum_{m=0}^{\infty}(-1)^m A_0^{(2m)} \frac{Fek_{2m}(\xi, -q)}{Fek_{2m}(\xi_0, -q)} ce_{2m}(\eta, -q) \tag{A8}$$

There are several representations of $Fek_{2m}(\xi, -q)$, but the one most suited to efficient calculation and providing uniform convergence in the ξ-plane is [*McLachlan*, 1947, p. 248]

$$Fek_{2m}(\xi, -q) = G_{2m}\sum_{r=0}^{\infty} A_{2r}^{(2m)} I_r(v_1(\xi)) K_r(v_2(\xi)) \tag{A9}$$

where $I_r(\ )$ and $K_r(\ )$ are, respectively, modified Bessel functions of the first and second kinds of orders r and $\nu_1(\xi) = \sqrt{q}\exp(-\xi)$, $\nu_2(\xi) = \sqrt{q}\exp(\xi)$. G_{2m} is a coefficient which cancels in the ratio of the solution for U_m in equation (A8). Its definition is given in the work of *McLachlan* [1947, p.248].

[65] To form the integral $\int_\Gamma \partial U_m/\partial n \, ds$, it is noted that, from the work of *McLachlan* [1947, p.172], $\partial U_m/\partial n = 1/l_1 \partial U_m/\partial \xi$ and $ds = l_1 \, d\eta$. Although $l_1 = 1/2(\cosh 2\xi - \cos 2\eta)$, it will not appear in the conversion of the integral to (ξ, η) coordinates. After substituting equations (A9) into (A8) then forming the derivative $\partial U_m/\partial \xi$, then

$$\int_\Gamma \frac{\partial U_m}{\partial n} ds = -4\pi U_c \sum_{m=0}^{\infty}\left[A_0^{(2m)}\right]^2 \cdot \left\{\frac{\sum_{r=0}^{\infty} A_{2r}^{(2m)}[v_1(\xi_0) I_{r+1}(v_1(\xi_0)) + v_2(\xi_0) K_{r+1}(v_2(\xi_0))]}{\sum_{r=0}^{\infty} A_{2r}^{(2m)} I_r(v_1(\xi_0)) K_r(v_1(\xi_0))}\right\} \tag{A10}$$

En route to this expression, $\int_0^{\pi/2} ce_{2m}(\eta, -q)\, d\eta = (-1)^m \pi/2A_0^{(2m)}$, and the identities $I_r'(\nu) = I_{r+1}(\nu) + r/\nu \, I_r(\nu)$ and $K_r'(\nu) = -K_{r+1}(\nu) + r/\nu \, K_r(\nu)$ have been used.

[66] Convergence in all the summations above is rapid, typically requiring 10–20 terms for 14 decimal place accuracy.

[67] The determination of separation constants e_{2m} and associated coefficients $A_{2r}^{(2m)}$ is now examined. When the series expression for $ce_{2m}(\eta, -q)$, given in equation (A5), is substituted in the differential equation (A3) and cosine coefficients are equated, an infinite series of coupled equations result which involve q, e, and A_{2r}, $r = 0, \ldots \infty$.

[68] Traditionally, as in the work of *McLachlan* [1947], e is first calculated from a transcendental equation involving infinite continued fractions for which there are infinite numbers of solutions, e_{2m}, $m = 0, \ldots \infty$. $A_{2r}^{(2m)}$ are then found by back substitution in terms of q, e_{2m}, and $A_0^{(2m)}$. The number of equations needed is not large, usually five more than that required in the summations of Mathieu functions. However, as *Vega* [2003] showed, the process is not straightforward numerically, requiring matching of low-order separation constant calculations with separate high-order calculations. A more recent approach is to pose the calculations as an eigenvalue-eigenvector problem [*Chaos-Cador and Ley-Koo*, 2002; *Stammes and Spjelkavik*, 1995; *Vega*, 2003]. The separation constants are the eigenvalues, and the A_{2r} coefficients become those of the eigenvectors. This particular approach used here is very straightforward, numerically robust, and eigenvalues and eigenvectors are calculated in one process using the complex valued routine CEIGV of EISPACK [*Smith et al.*, 1976].

[69] Although the constants $A_0^{(2m)}$ can be absorbed into the coefficients B_{2m}, it is convenient to use scale factors

$$s_{2m} = \left\{2\left[A_0^{(2m)}\right]^2 + \sum_{r=1}^{\infty}\left[A_{2r}^{(2m)}\right]^2\right\}^{1/2} \tag{A11}$$

so that $A_{2r}^{(2m)}$ are replaced by $A_{2r}^{(2m)}/s_{2m}$. This then produces the standard normalization

$$1 = 2\left[A_0^{(2m)}\right]^2 + \sum_{r=1}^{\infty}\left[A_{2r}^{(2m)}\right]^2 \tag{A12}$$

upon which are based the identities used to obtain the solution for U_m.

[70] It has been tacitly assumed that the eigenvalues are single valued. This is true for q real. However, for q complex, double-valued eigenvalues may occur at discrete q. An extensive set of tables produced by *Blanch and Clemm* [1969] show that these eigenvalues are not closely spaced. Should these repeated eigenvalues occur during calculations, the normalization expression (A12) cannot be formed [*Abramowitz and Stegun*, 1965, p.732], and the expression (A7) for B_{2m} will not be valid. However, this difficulty can be avoided by changing values of p (thence q), done by changing the number of terms selected in the Talbot-Green, Laplace transform inversion method.

[71] **Acknowledgments.** Funding for this research was provided in part by the Natural Sciences and Engineering Research Council of Canada, Cameco Ltd. and the Saskatchewan Potash Producers Association.

References

Abramowitz, M., and I. A. Stegun (1965), *Handbook of Mathematical Functions*, pp. 1046, Dover, Mineola, N. Y.

Blanch, G., and D. S. Clemm (1969), The double points of Mathieu's differential equation, *Math. Comput.*, *23*, 97–108.

Boldt-Leppin, B. E. J., and M. J. Hendry (2003), Application of harmonic analysis of water levels to determine vertical hydraulic conductivities in clay-rich aquitards, *Ground Water*, *41*(4), 514–522.

Carslaw, H. S., and J. C. Jaeger (1959), *Conduction of Heat in Solids*, pp. 510, Oxford Univ. Press, New York.

Chaos-Caldor, L., and E. Ley-Koo (2002), Matrix evaluation revisited: Matrix evaluation and generating functions, *Rev. Mex. Fis.*, *48*(1), 67–75.

Christiansen, E. A. (1971), Tills in southern Saskatchewan, Canada, in *Till: A symposium*, edited by R. P. Goldthwait, pp. 402, Ohio State Univ. Press, Columbus.

Christiansen, E. A. (1986), Geology of Luck Lake irrigation project, *Rep. 0114-002*, Sask. Water Corp., Moose Jaw, Saskachewan, Can.

deHoog, F. R., J. M. Knight, and A. N. Stokes (1982), An improved method for the Laplace inversion problem, *SIAM J. Stat. Comput.*, *3*, 357–366.

Fetter, C. W. (1999), *Contaminant Hydrogeology*, 500 pp., Prentice-Hall, Upper Saddle River, N. J.

Gelhar, L. W., C. Welty, and K. R. Rehfeldt (1992), A critical review of data on field-scale dispersion in aquifers, *Water Resour. Res.*, *28*(7), 1955–1974.

Gerber, R. E., J. I. Boyce, and K. W. F. Howard (2001), Evaluation of heterogeneity and field-scale groundwater flow regime in a leaky till aquitard, *Hydrogeol. J.*, *9*, 60–78.

Grisak, G. E., and J. F. Pickens (1980), Solute transport through fractured media. 1: The effect of matrix diffusion, *Water Resour. Res.*, *16*(4), 719–730.

Harrington, G. A., and M. J. Hendry (2005), Chemical heterogeneity in diffusion-dominated aquitards, *Water Resour. Res.*, *41*(12), W12432, doi:10.1029/2004WR003928.

Harrington, G. A., and M. J. Hendry (2006), Using direct-push EC logging to delineate heterogeneity in a clay-rich aquitard, *Ground Water Monit. Rem.*, *26*(1), 92–100.

Harrison, B., E. A. Sudicky, and J. A. Cherry (1992), Numerical-analysis of solute migration through fractured clayey deposits into underlying aquifers, *Water Resour. Res.*, *28*(2), 515–526.

Hazen, A. (1892), Some Physical Properties of Sand and Gravels, pp. 539–556, Mass. State Board of Health, Ann. Rep.

Hendry, M. J. (1982), Hydraulic conductivity of a glacial till in Alberta, *Ground Water*, *20*(2), 162–169.

Hendry, M. J., and L. I. Wassenaar (1999), Implications of the distribution of δD in pore waters for groundwater flow and the timing of geologic events in a thick aquitard system, *Water Resour. Res.*, *35*(6), 1751–1760.

Hendry, M. J., and L. I. Wassenaar (2000), Controls on the distribution of major ions in pore waters of a thick surficial aquitard, *Water Resour. Res.*, *36*(2), 503–513.

Hendry, M. J., and L. I. Wassenaar (2005), Origin and migration of dissolved organic carbon fractions in a clay-rich aquitard: 14C and δ13C evidence, *Water Resour.*, 41.

Hendry, M. J., L. I. Wassenaar, and T. Kotzer (2000), Chloride and chlorine isotopes (36Cl and δ37Cl) as tracers of solute migration in a thick, clay-rich aquitard system, *Water Resour. Res.*, *36*(1), 285–296.

Hendry, M. J., C. J. Kelln, L. I. Wassenaar, and J. Shaw (2004), Characterizing the hydrogeology of a complex clay-rich aquitard system using detailed vertical profiles of the stable isotopes of water, *J. Hydrol.*, *293*, 47–56.

Hvorslev, M. J. (1951), Time lag and soil permeability in ground-water observations, Bull. No. 36, pp. 1–50, U.S. Army Corps, Vicksburg, Mississippi.

Jørgensen, P. R., L. D. McKay, and J. P Kistrup (2004), Aquifer vulnerability to pesticide migration through till aquitards, *Ground Water*, *42*(6), 841–855.

Kucuk, F., and W. E. Brigham (1979), Transient flow in elliptical systems, *SPE J.*, 401–410.

Lever, D. A., and M. H. Bradbury (1985), Rock-matrix diffusion and its implications for radionuclide migration, *Mineral. Mag.*, *49*, 245–254.

Maloszewski, P., and A. Zuber (1985), On the theory of tracer experiments in fissured rocks with a porous matrix, *J. Hydrol.*, *79*(3–4), 333–358.

Maloszewski, P., and A. Zuber (1990), Mathematical modeling of tracer behavior in short-term experiments in fissured rocks, *Water Resour. Res.*, *26*(7), 1517–1528.

Maloszewski, P., and A. Zuber (1991), Influence of matrix diffusion and exchange reactions on radiocarbon ages in fissured carbonate aquifers, *Water Resour. Res.*, *27*(8), 1937–1945.

McKay, L. D., R. W. Gillham, and J. A. Cherry (1993), Field experiments in a fractured clay till. 2: Solute and colloid transport, *Water Resour. Res.*, *29*(12), 3879–3890.

McLachlan, N. W. (1947), *Theory and Application of Mathieu Functions*, 401 pp., Clarendon, Oxford, U.K.

Neretnieks, I. (1980), Diffusion in the rock matrix: An important factor in radionuclide retardation?, *J. Geophys. Res.*, *85*(B8), 4379–4397.

Neretnieks, I. (1981), Age dating of groundwater in fissured rock: influence of water volume in micropores, *Water Resour. Res.*, *17*(2), 421–422.

Obut, S. T., and T. Ertigen (1987), A composite system solution in elliptic flow geometry, *SPE Form. Eval.*, 227–236, Sept.

Piessens, R., and R. Huysmans (1984), Algorithm 619: Automatic numerical inversion of the Laplace transform, *Trans. Math. Software*, *10*, 348–353.

Robinson, P. C., and P. R. Maul (1991), Some experience with the numerical inversion of Laplace transforms, *Math. Eng. Ind.*, *3*, 111–131.

Robinson, N. I., and J. M. Sharp Jr. (1997), Analytical solution for contaminant transport in a finite set of parallel fractures with matrix diffusion, *CSIRO Mathematical and Information Sciences Report CMIS-C23*, Commonwealth Scientific and Industrial Research Organisation, Adelaide.

Robinson, N. I., J. M. Sharp Jr., and I. Kriesel (1998), Contaminant transport in sets of parallel fractures with fracture skins, *J. Contam. Hydrol.*, *31*, 83–109.

Shaw, J. (1997), Hydrogeology of a thick clay-rich till and Cretaceous bedrock clay sequence in Saskatchewan, Canada, *M. Sc. thesis, University of Saskatchewan*.

Shaw, R. J., and M. J. Hendry (1998), Hydrogeology of a thick clay till and Cretaceous clay sequence. Saskatoon, Saskatchewan, Canada, *Can. Geotech. J.*, *35*, 1041–1052.

Smith, B. T., J. M. Boyle, J. J. Dongarra, B. S. Garbow, Y. Ikebe, V. C. Klema, and C. B. Moler (1976), Matrix eigensystem routines–EISPACK guide, *Lecture Notes in Computer Science*, vol. 6, Springer, New York.

Spath, J. B., and R. K. M. Thambynayagam (1997), Well test solutions for vertically fractured injection wells, *Transp. Porous Media*, *29*, 27–45.

Stammes, J. J., and B. Spjelkavik (1995), New method for computing eigenfunctions (Mathieu functions) for scattering by elliptic cylinders, *Pure Appl. Opt.*, *4*, 251–262.

Stanislav, J. F., C. V. Easwaran, and S. L. Kokal (1987), Analytical solutions for vertical fractures in a composite system, *J. Can. Petrol. Technol.*, *26*(5), 51–56.

Stanislav, J. F., C. V. Easwaran, and S. L. Kokal (1992), Elliptical flow in composite reservoirs, *J. Can. Petrol. Technol.*, *31*(10), 47–50.

Sudicky, E. A., and E. O. Frind (1981), Carbon 14 dating of groundwater in confined aquifers: Implications of aquitard diffusion, *Water Resour. Res.*, *17*(4), 1060–1064.

Sudicky, E. A., and E. O. Frind (1982), Contaminant transport in fractured porous media: analytical solutions for a system of parallel factures, *Water Resour. Res.*, *18*(6), 1634–1642.

Talbot, A. (1979), The accurate numerical inversion of Laplace transforms, *J. Inst. Math. Appl.*, *23*, 97–120.

Tang, D. H., E. O. Frind, and E. A. Sudicky (1981), Contaminant transport in fractured porous media: Analytical solution for a single fracture, *Water Resour. Res.*, *17*(3), 555–564, Errata: Davis, G. B. and C. D. Johnston (1984), *Water Resour. Res*., 20, 1321–1322.

Vega, J. C. G. (2003), Theory and Numerical Analysis of the Mathieu Functions, http://homepages.mty.itesm.mx/jgutierr (accessed August 25, 2006).

Vengosh, A., and M. J. Hendry (2001), Chloride-bromide-δ^{11}B systematics of a thick clay-rich aquitard system, *Water Resour. Res.*, *37*(5), 1437–1444.

Wassenaar, L. I., and M. J. Hendry (2000), Mechanisms controlling the distribution and transport of 14C in a clay-rich till aquitard, *Ground Water*, *38*(3), 343–349.

Yan, X.-P., R. Kerrich, and M. J. Hendry (2001), Distribution of the rare earth elements in porewaters from a clay-rich aquitard sequence. Saskatchewan, Canada, *Chem. Geol.*, *176*, 151–172.

G. A. Harrington and M. J. Hendry, Department of Geological Sciences, University of Saskatchewan, 114 Science Place, Saskatoon, SK S7N 5E2, Canada. (harrington.glenn@saugov.sa.gov.au)

N. I. Robinson, School of Chemistry, Physics and Earth Sciences, Flinders University, GPO Box 2100, Adelaide, SA 5001, Australia.